

On-chip integration of ultra-thin glass cantilever for physical property measurement activated by femtosecond laser impulse

Tao Tang, Yansheng Hao, Yigang Shen, Yo Tanaka, Ming Huang, Yoichiro Hosokawa, Ming Li and Yaxiaer Yalikus

Abstract— Under the excitation of acoustic radiation, the amount of energy absorbed and rebounded by cells have the relationship with mechanical properties, e.g. stiffness, shape, weight and so on. In this paper, a femtosecond laser-activated micro-detector is designed to convert this relationship into an electrical signal. First, the acoustic radiation is generated by a femtosecond laser pulse in a microchannel and acts on neighbor cells / beads. Then, an ultra-thin glass sheet (UTGS)-based pressure sensor (cantilever) is fabricated at the bottom of the microfluidic chip to monitor changes in acoustic pressure during detection process. In this detection system, the pressure sensor is fabricated with a 10 μm UTGS in a shape of rectangular cantilever and functions like a detector to convert acoustic waves into shift response. Based on the amplitude of detected pulses, we can directly analyze the acoustic energy, coming from either femtosecond laser pulse or that remains after penetrating target cells. We have taken experiments on 10 μm beads and verified the applicability of this micro-detector, and the proposed method has great potential to be applied in label-free cell manipulation (i.e., sorting) as a detection mechanism.

I. INTRODUCTION

Cellular analysis brings critical knowledge to modern biology and clinical sciences. The in-depth exploration of cellular behavior with information about their properties lays a scientific foundation for cell biology, drug development, and the disease diagnosis[1], [2]. In general, different types of cells may differ in mechanical properties (i.e. stiffness or shape), which is also a key biomarker for the tumor cell identification.

To date, conventional cellular analysis mainly focusses on employing the atomic force microscopy (AFM), constricted channels or sheath flow to analyze the cell's stiffness (or deformability). However, the first one is limited by its low throughput (< 100 cells per hour), and others have requirements on the cell's size, especially the constriction channels are risky to damage cells[3], [4]. Herein, we proposed a contactless method – femtosecond (fs) laser-induced acoustic detection and designed a detector with a 10

μm ultra-thin glass sheet (UTGS) cantilever. Specifically, the radiation of a fs-laser pulse at the focal point in fluids results in the formation of a cavitation bubble and the acoustic radiation (i.e. shock wave and stress wave) [5], [6]. The whole process occurs on a typical time scale of tens of microseconds[7]. Besides, based on the past research by our team, we have found that the acoustic radiation will pass through neighbor cells / beads, which results in the acoustic energy attenuation. Importantly, the attenuation of the propagating acoustic energy see a direct relationship with the cell/bead's size and stiffness[8].

However, this detection in the past was only applicable to AFM, and in order to achieve a high efficiency, we proposed to design a microfluidic-based cell characterization system, which enables the characterization of these properties of sequential cells in suspension. Here, we took advantage of the working principle of AFM and fabricated a cantilever on an UTGS that was placed on the bottom of a microfluidic channel. The cantilever can work as a pressure sensor to quantify the acoustic energy in the form of cantilever bending. Besides, unlike other types of flexible materials for microfluidic sensors, UTGS ($\sim 10 \mu\text{m}$ in this case) has better chemical and physical stability and can be reused after being cleaned. As for the thickness, polydimethylsiloxane (PDMS) film[9] is typically limited to about 100 μm in the case of manual handling, and polymers[10], [11] and plastics[12], [13] are, respectively, limited to about 100 μm and 25 μm . For the fabrication process, the complexity of fabricating about 10 μm PDMS sheets is much bigger than that of an UTGS. Besides, our team, so far, has conducted abundant research in the fabrication and application of the UTGS [14].

Theoretically, the amplitude and duration of the collected signal are tightly related to the cell's flowing speed, size and stiffness. In this paper, the relationship with the flowing speed has been verified in experiments, and some metrics are also provided to analyze collected data from a statistics perspective. Notably, the proposed method is also the first research by far to analyze the cellular properties under the laser-induced acoustic radiation.

II. PRINCIPLE

A. Generation of acoustic radiation

In laser ablation, when a fs-laser pulse is triggered at the focal point, an ablation plasma is generated within several hundred pico-seconds after laser pulse irradiation[15] then results in the generation of cavitation bubbles. In general, the dynamics of the cavitation bubble in fluids consist of a series of damping phenomena [5], [6] (e.g. formation, expansion, collapse and rebound). Theoretically, the damping oscillation of a spherical bubble in a compressible liquid can be

Tao Tang, Yoichiro Hosokawa and Yaxiaer Yalikus are with the Graduate School of Material Science, Nara Institute of Science and Technology, 8916-5 Takayama-cho, Ikoma, Nara 630-0192, JAPAN (corresponding author to e-mail: tang.tao.ts3@ms.naist.jp)

Yigang Shen and Yo Tanaka are with Center for Biosystems Dynamics Research (BDR), RIKEN, 1-3 Yamadaoka, Suita, Osaka 565-0871, Japan

Ming Huang is with the Graduate School of Information Science, Nara Institute of Science and Technology, 8916-5 Takayama-cho, Ikoma, Nara 630-0192, JAPAN

Ming Li, School of Engineering, Macquarie University, Sydney, 2109, Australia (ming.li@mq.edu.au)

expressed approximately by the Rayleigh-Plesset equation[16]:

$$R\ddot{R} + \frac{3}{2}\dot{R}^2 = p_{g0}\left(\frac{R_0}{R}\right)^{3\lambda} - 1 - \frac{2We}{R} - \frac{4}{Re}\frac{\dot{R}}{R} \quad (1)$$

where radius R is a function of time ($R(t)$), and R_0 , \dot{R} and \ddot{R} respond to the initial radius, velocity, and acceleration of the bubble, respectively. p_{g0} denotes the initial gas pressure inside the bubble, which is calculated from the hydrostatic pressure (p_∞), and the vapor pressure inside the bubble (p_v), based on a formula: $p_{g0} = \varepsilon \cdot (p_\infty - p_{g0})$. The Weber number (We) is defined with gas adiabatic index (γ) as $We = (p_\infty - p_v)R_0 / \gamma$. But the Eq. (1) does not account for the energy radiated as acoustic waves. This is a numerical study to analyze the effects of liquid bulk viscosity on bubble dynamics, so that all lost energy is due to the fluidic viscosity. We can approximate the bubble dynamics by choosing relatively small Reynolds number (Re). The acoustic radiation normally occurs at the formation or collapse of a bubble system. At this stage, the temperatures (up to 20000K) and inertial pressure (several thousand bars) inside the bubble comes to an extraordinary condition[6]. This leads to an impulse pressure onto neighbor liquids and forms a shock wave. On the outside of bubble wall, the pressure (p), while initial expansion or bubble collapse starts, can be formulated as[17]

$$p = \frac{3}{2}\dot{R}^2\rho - p_\infty\left(1 - \frac{R_0^3}{R^3}\right) \quad (2)$$

The parameters[18], [19] involved in this case are chosen as $R_0 = 0.1$ mm, $\varepsilon = 100$, $p_\infty = 100$ kPa, $p_v = 2.33$ kPa, $\gamma = 0.073$ $N\cdot m^{-1}$, $\rho = 1000$ $kg\cdot m^{-3}$, $\lambda = 1.4$, $\kappa = 1.667$ and $Re = 50$. The Eq. (1) is integrated by explicating Runge-Kutta method of order 5(4)[20] to obtain R and \dot{R} . And then, the calculations are performed for Eqs. (2) to obtain the emitted pressure of the bubble system.

There is no physical significance for the timescale and amplitude obtained here, since all equations are rough descriptions of bubble dynamics. Therefore, we normalize all resolved parameters (e.g. $R(t)$, $\dot{R}(t)$, $E(t)$ and $p(t)$) into dimensionless parameters. Here, they all are normalized by the global maximum over the whole period, and the time axis (t) is normalized by the duration (t_c) of the first oscillation cycle.

Fig. 1(a) shows the temporal variation of radius of the laser-induced bubble. Besides, as the bubble oscillates, the velocity of the bubble wall undergoes sudden changes at some critical points (collapse or initial expansion of the bubble), where the cavitation bubble will release a large amount of energy in the form of acoustic radiation. Some research [19], [21], [22] have pinpointed out that during the damping oscillation, most of the energy[23] (70% ~ 90%) turns into shock waves, which is also the main components of the acoustic radiation. This phenomenon means the generation of shock pulse at critical points, which is also supported by the solution of Eq. (2) (see Fig. 1(b)). We can assume that the first pulse induced by the initial expansion is

significantly larger than others, which is also widely used in bio-experiments[6], [24], [25]. Besides, the waveforms of shock pressure in Fig. 1(b) are pulse in theories, so we assume that, based on the result, the laser-induced acoustic radiation can be treated as a pulse wave.

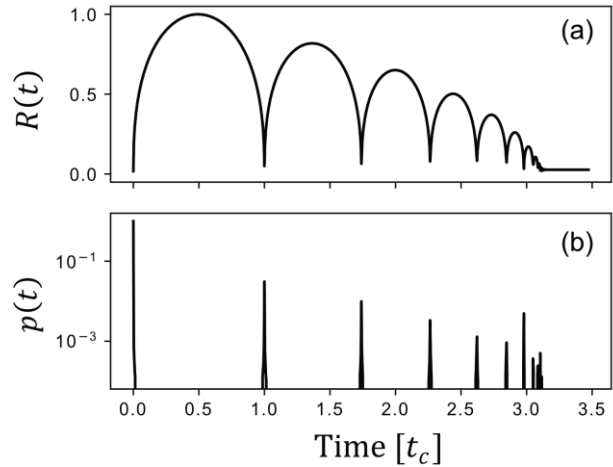


Fig.1: Time history for the dynamics of a spherical bubble oscillating in an infinite viscous liquid, as determined by Rayleigh-Plesset equation; (a) The time evolution of bubble radius ($R(t)$); (b) The semi-log graph of the time evolution of the pressure ($p(t)$) at the bubble wall.

Additionally, in practical analysis, the stress wave coming from oscillating phases of the bubble can be neglected, especially in the flowing fluids, as the energy of shock wave is considerably larger than that of stress wave. The application of the fs-laser induced shock wave can be found in the research of Iino et al.[26] for cell sorting. The theoretical upper limit of throughput can reach 100 kHz, in the case of microparticle with a space of 10 μm , flowing at a speed of 1 $m\cdot s^{-1}$. This research paves the foundation for our method to achieve a high efficiency cell detector.

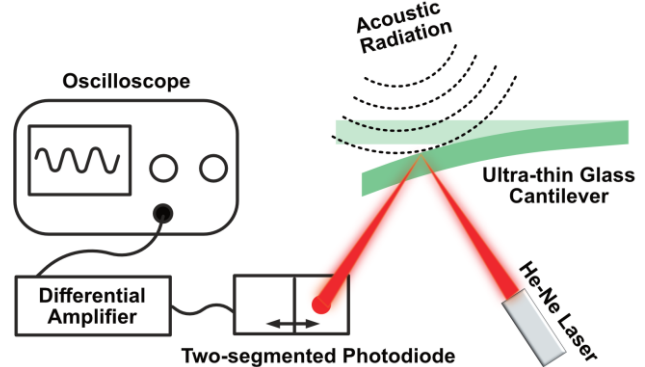


Fig.2: Schematic image of basic principle of measuring displacement of the UTGS cantilever using principle of position sensor.

B. Principle of UTGS detector

To quantify the acoustic energy in microfluidics, we took advantage of the working principle of AFM and designed a cantilever detector on a 10 μm UTGS. As shown in Fig. 2, a laser beam (He-Ne laser) is focused on the upper surface of the cantilever, such that the cantilever bending can represent the acoustic force acting on the cantilever and be monitored by the shift of the He-Ne laser focal point.

Through this way, the acoustic-induced displacement of the cantilever is transferred into electric signals and recorded by an oscilloscope. Once an acoustic radiation (a shock wave) hits the upper surface of the cantilever, and the cantilever shows a downward trend. The degree of deformation increases together with the increase in acoustic strength.

C. Principle of UTGS detector

The detection system includes a PDMS microfluidic chip integrated with a 10 μm UTGS inside (Fig. 3(c)), as well as a differential amplifier. Obviously, there is a 10 μm gap etched under the cantilever for the downward bending. When a cell is flowing above the cantilever, a fs-laser pulse is triggered, and then both types of acoustic waves will act on the cantilever, including laser-induced shock wave and the wave passing through cells or rebounding at the surface. Theoretically, there will be two pulse (Fig. 3(d)) detected in the detection system, once a cell responds to the laser-induced acoustic radiation. If not, there will be only one pulse, which has also been verified in experiments.

Fig. 3(a) depicts the generation of the response wave of a cell and the fs-laser induced acoustic wave, both acting on the cantilever sequentially. The cell near the focal point will respond to such acoustic pulse, where part of the energy will be attenuated inside the cell as passing through, while other parts will be rebounded by the cell surface. Given different propagation trajectories and mediums, the response wave of each cells should also vary in strength and delay to the original pulse. Besides, the difference in the response wave can appear as a change in the bending level of the cantilever. As for the energy consumed during propagation, we can attribute it to the different stiffness and shapes of cells/beads. The loss of acoustic energy can be calculated from the difference in the amplitude of the original pulse to the response wave (Fig. 3(d)). Here, two important parameters are involved, namely the distance between the target cell and the focal point, and the pulse energy. The fs-laser pulse with high energy is possible to push the target cell away or physically damage the cell. However, the pulse with low energy might not be enough to induce the cell's response. The determination of both parameters is quite critical in this research.

Fig. 3(b) is the top view of the detection system. To detect a large number of cells sequentially, the distance between the two cells should be selected according to the length of the cantilever. Herein, considering the dimension of the cantilever fabricated, it is quite difficult to realize that there is only one cell above the cantilever each time. Therefore, we will neglect the effect of multiple cells above

the cantilever at current stage, which will be analyzed in the future research.

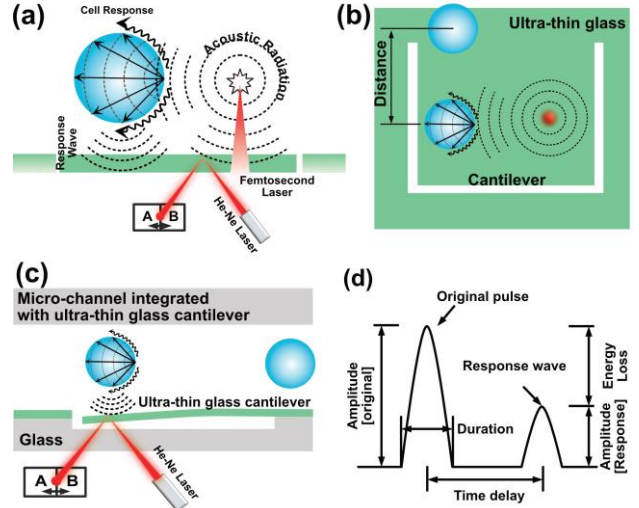


Fig.3: Schematics of the femtosecond laser-induced acoustic radiation and cell's response. (a) Front view of detection system; (b) Top view of this system; (c) Side view of the detection system; (d) Explanation of the detected signal.

III. NUMERICAL SIMULATION

To validate the relation between the acoustic radiation and the deformation level of cantilever in a microchannel. We simplify the acoustic radiation as a pulse force acting on the cantilever in the form of Gaussian distribution. A simplified microchannel ($500 \times 300 \times 30 \mu\text{m}$) and a cantilever (4 or 10 μm in depth) are built in COMSOL 5.4b (COMSOL Inc., USA) and solved in solid-fluid module.

Fig. 4(a) shows the simulation model used for analysis in COMSOL, and there is a cantilever with a constant width of 100 μm . Neglecting the energy exhausting during propagation, we applied a transient force of $2 \times 10^{-12} \text{ N}\cdot\text{s}$ on the front of the cantilever[27]. The correlation of the oscillation amplitude to the cantilever length is depicted in Fig. 4(b) and (c). Obviously, under the same force, thinner glass tends to produce greater deformation. In these cases, a cantilever with 4 μm depth can reach a maximal amplitude of almost 0.6 μm , and that with 10 μm can reach 0.08 μm . Theoretically, it is more detectable for the oscillation amplitude on the application of a thinner glass cantilever. However, the 4 μm glass cantilever oscillates at its first natural frequency (Fig. 4(c)), which significantly complexes the latter analysis and leads to a low efficiency, as we have to wait until the vibration stops before the next detection. Besides, in a real experiment, the application of the UTGS is limited by the fabrication technique, because the complexity of applying a 4 μm glass is much bigger than that of 10 μm . Therefore, in our experiment, we applied an UTGS of 10 μm rather than 4 μm .

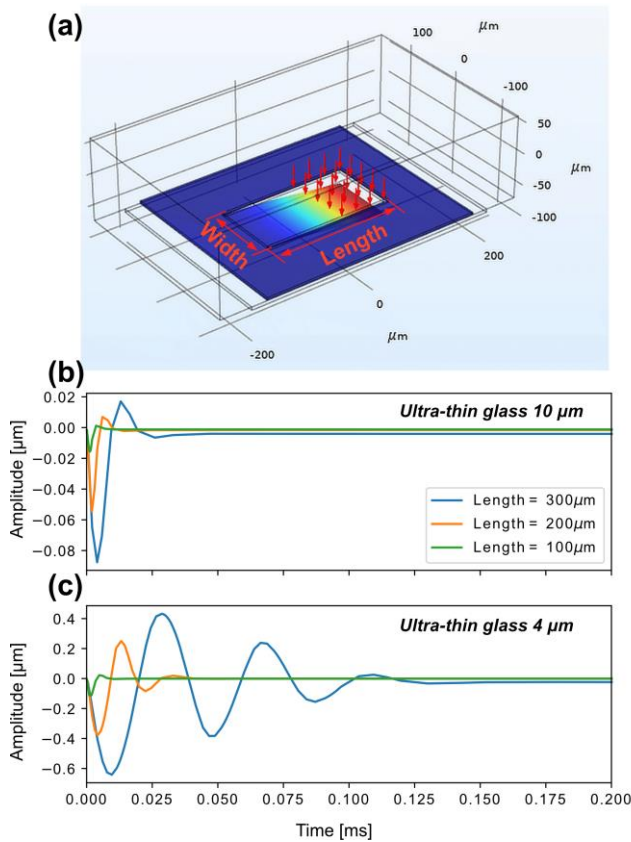


Fig.4: Numerical simulation of the impulse response as a function of the cantilever length. (a) Simulation model. Different shift response at different cantilever length, including 10 μm (b) and 4 μm (c).

IV. EXPERIMENTAL SETUP

The working principle of the proposed fs laser-induced detection system has been introduced in previous sections. And the microfluidic chip consists of three layers (Fig. 5): the top layer PDMS channel (Top Layer), an UTGS (Middle Layer), a glass substrate (Bottom Layer). Fig. 5(a-d) illustrates the fabricating flow for the top layer. The mode was formed by one layer of SU-8 photoresist (Su-8 3050, Tokyo Ohka Kogyo, Tokyo, Japan) with a 40 μm high on a Si wafer (4-inch diameter). Next, uncured PDMS (SYLGARD 184, Dow Corning, Midland, MI, USA) was poured onto the SU-8 mode and cured at 80 $^{\circ}\text{C}$ for 3 hours. After curing, holes were punched through the top part to form fluid inlets and outlets.

The PDMS microchannel and an UTGS are bonded together, in Fig. 5(d). Then, a femtosecond laser (Solstice Ace100F; Spectra Physics, Santa Clara, CA) is used to cut a cantilever shape on the boned UTGS. The parameters of femtosecond laser involved are 800 nm wavelength, 100 fs pulse width, and 1 kHz repetition rate. The laser pulse energy (1.1 $\mu\text{J}/\text{pulse}$) used in this work is determined based on our past research[28], [29], following the requirement to minimize the nano-debris generation during processing. Through a programmable electromotive stage (BIOS-206T; Sigmakoki, Tokyo), a microscope (Olympus IX71; Olympus Inc. Tokyo), and the 20x objective lens, a rectangular cantilever (141 \times 212 μm) was fabricated as shown in Fig.

5(g) and Fig. 6(b), which was placed in the center of the channel.

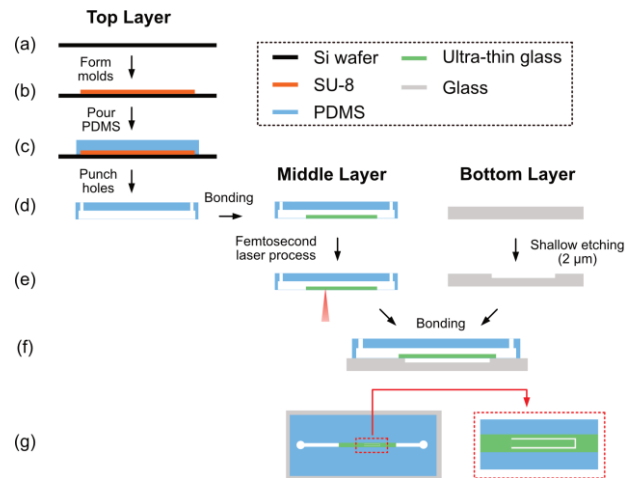


Fig.5: Process flow of the prototype chip device integrated with UTGS. (a) Si wafer as substrates for modes; (b) Forming Su-8 modes; (c) Pour PDMS onto the SU-8 mode; (d) Remove PDMS from the mode. Inlet and outlet holes are punched in the top layer. An UTGS is then bonded to the PDMS. (e) For middle layer, cantilever is fabricated on the UTGS using femtosecond laser. For bottom layer, a gap of 2 μm is etched on glass substrate. (f) PDMS, UTGS and Glass substrate are bonded together using plasma bonding. (g) Top view and partial enlarged view of the prototype chip device

Additionally, in Fig. 5(d) for the bottom layer, soft lithography and wet etching process are used to fabricate a shallow gap (2 μm) in a glass substrate (Fig. 5(e)), so as to leave enough space for the downward bending of the cantilever. Next, the glass sheets are chemically cleaned. The chemical cleaning process uses piranha solution containing sulfuric acid and hydrogen peroxide at a ratio of 3:1. After 20 min chemical cleaning, the glass sheets are removed from the solution and rinsed with ultra-pure water for 10 min. Finally, the glass substrate is thoroughly dried with a nitrogen air gun (5 min) in a draft chamber. Three layers are exactly aligned and bonded together (Fig. 4 (f-g)).

V. EXPERIMENTAL RESULT

Measurements have been performed with polymer beads of 10 μm (Polysciences, Inc., #17136-5) that were diluted in DI water with a concentration of 1×10^4 particles/ml. Then, the diluted beads were flown through the microchannel detection area at a speed of about 1 mm/s, which is a relatively slow speed at current stage to make sure if the bead trajectory changes under the laser irradiation. A fs-laser (Spectra-Physics Solstice-Ace, 800nm, 100fs, 20Hz) was focused at a point of about 10 μm higher than the cantilever. A customized shutter was applied to enable each laser

radiation last 20 μs . The bending movement of the cantilever was monitored and directly recorded by an oscilloscope (GDS-3154 GW INSTEK) with a sampling frequency (250 kHz).

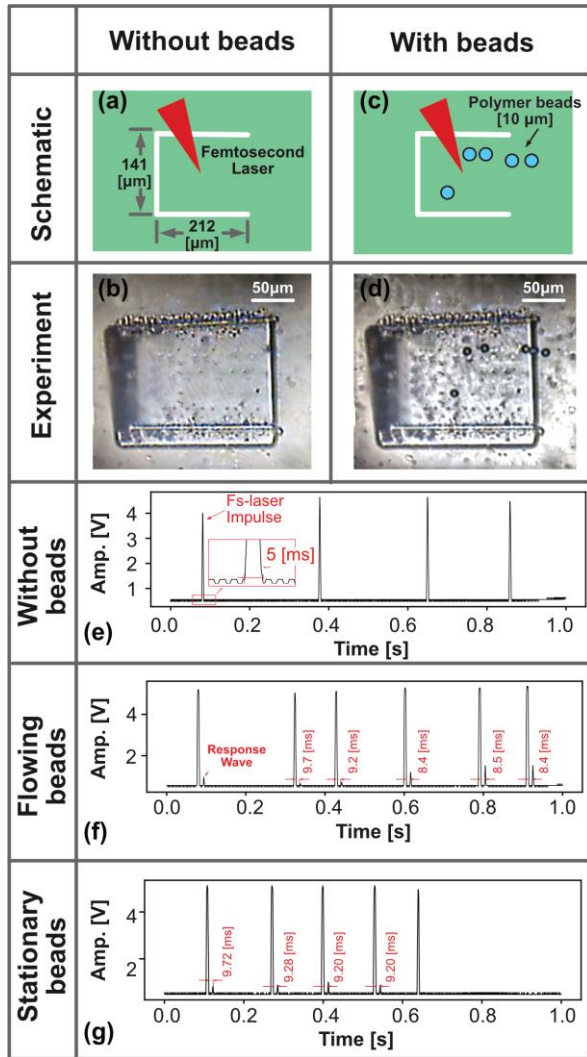


Fig.6: Schematic illustration of the UTGS cantilever with (a) or without beads (b) above it. (c-d) the fabricated glass cantilever in real experiment with or without beads above it; (e) pulse signal recorded without the beads around the focal point; (f) pulse and response signal recorded with flowing beads; (g) pulse and response signal recorded with stationary beads above the cantilever.

As shown in Fig. 6, by far, we have conducted the experiment in two cases: with or without beads above the cantilever. When there are no beads within detection area, the fs laser pulse cannot stimulate any response wave, in Fig. 6(e). In contrast, once the bead comes close to the focal point above cantilever, the response wave is emerging and seems like a small tail to the original pulse. As shown in Fig. 6(f), we randomly shot laser pulses into a high-concentration beads flow, and we found that the time delay between the original pulse and response wave is related to the amplitude

of the response wave. The shorter the time delay between the original pulse and the response wave, the higher the amplitude of the response wave. This should be due to the energy loss during propagation in fluids.

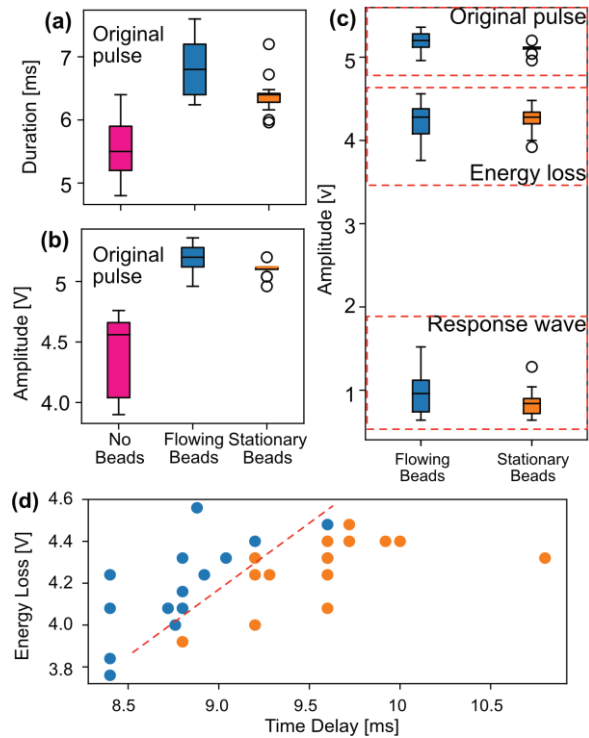


Fig.7: Statistic analysis based on the recorded signal; (a) duration of the original pulse; (b) amplitude of the recorded original pulse signal; (c) amplitude distribution of the measured signal in terms of the original pulse, response wave and energy loss; (d) scatter plot of relationship between the time delay and the energy loss.

Additionally, from a statistic perspective, we found that the existence of the flowing / stationary beads during detection tends to greatly extend the time duration of original pulse (Fig. 7(a)). At the same time, the amplitude of original pulse detected will also be enhanced. At current stage, we attributed this result to the rebound wave occurring at the surface of beads, which merge with the original pulse and both act on the cantilever simultaneously. This assumption can also be applied to explain why the distribution variance of flowing beads is bigger than that of stationary beads. Due to the Doppler effect, when the original pulse is bounded back by a moving bead, both the frequency and amplitude of the rebound wave will change. This modification is related to the speed of the moving beads. As a result, moving beads have a bigger contribution to extending the duration and amplitude of the detected original pulse compared to stationary ones, but the speed of each beads is different in this experiment, leading to a big variance in both parameters (i.e. duration and amplitude), as shown in Fig. 7 (a-b).

As shown in Fig. 7(c), we presented three describable metrics in a same plot, including the detected amplitude of the original pulse, response wave and energy loss between both pulses. As explained before, a big variance is observed in all three metrics in the case of flowing beads. Notably, the

median values of all three metrics produced by the flowing beads are discriminable from those of stationary beads. Additionally, in Fig. 7(d), a scatter plot of the flowing / stationary beads was provided based on the relationship between the energy loss and time delay. There is a clear distinction between both cases, which can be applied to distinguish cells / beads of different speeds.

VI. CONCLUSION

In this paper, we proposed a fs-laser induced detection system which has potential for single cell characterization. And the proposed system takes advantage of the working function of AFM and applies the technique of laser position detection to monitor the oscillation of the UTGS made cantilever. Theoretically, the UTGS-based sensor is of high sensitivity to sense the acoustic waves coming from either the fs-laser pulse or the cell's response. Compared with other detection systems, the proposed system has the possibility to be the first investigation on the cell's response to acoustic radiation, which will be verified in the following research. Besides, the total system is a transparent device, which enables the integration with other microfluidic systems like a photo detection system.

By far, we have found that the flowing speed is a key factor in this detection system due to the Doppler effect of the moving cells/beads. The flowing beads will interact with the fs-laser induced acoustic radiation, which can be monitored by the detection system. To further clarify the effect of cells / beads' size and stiffness on these provided metrics, more experiments are required to find a solid research conclusion. Therefore, in the future plan, we are going to modify the detection system to eliminate the influence of flow speed and focus the effect of the size and stiffness of cells/beads to both types of pulses (i.e., original pulse and response wave).

REFERENCES

- [1] J. Zhu and W. E. Paul, "Heterogeneity and plasticity of T helper cells," *Cell Research*, 2010, doi: 10.1038/cr.2009.138.
- [2] R. M. Welsh and L. K. Selin, "No one is naive: The significance of heterologous T-cell immunity," *Nature Reviews Immunology*, 2002, doi: 10.1038/nri820.
- [3] J. M. Kwan, Q. Guo, D. L. Klyuik-Price, H. Ma, and M. D. Scott, "Microfluidic analysis of cellular deformability of normal and oxidatively damaged red blood cells," *Am. J. Hematol.*, 2013, doi: 10.1002/ajh.23476.
- [4] M. Urbanska *et al.*, "A comparison of microfluidic methods for high-throughput cell deformability measurements," *Nat. Methods*, 2020, doi: 10.1038/s41592-020-0818-8.
- [5] Q. Wang, W. Liu, A. M. Zhang, and Y. Sui, "Bubble dynamics in a compressible liquid in contact with a rigid boundary," *Interface Focus*, vol. 5, no. 5, pp. 1–12, 2015, doi: 10.1098/rsfs.2015.0048.
- [6] H. Nazari-Mahroo, K. Pasandideh, H. A. Navid, and R. Sadighi-Bonabi, "How important is the liquid bulk viscosity effect on the dynamics of a single cavitation bubble?," *Ultrason. Sonochem.*, vol. 49, pp. 47–52, 2018, doi: 10.1016/j.ulsonch.2018.07.013.
- [7] P. A. Quinto-Su, H. H. Lai, H. H. Yoon, C. E. Sims, N. L. Allbritton, and V. Venugopalan, "Examination of laser microbeam cell lysis in a PDMS microfluidic channel using time-resolved imaging," *Lab Chip*, vol. 8, no. 3, pp. 408–414, 2008, doi: 10.1039/b715708h.
- [8] R. Yasukuni *et al.*, "Pulsed-laser-activated impulse response encoder (PLAIRE): detection of core-shell structure of biomimetic micro gel-sphere," *Appl. Phys. A Mater. Sci. Process.*, 2018, doi: 10.1007/s00339-018-2016-4.
- [9] J. H. Koschwanetz, R. H. Carlson, and D. R. Meldrum, "Thin PDMS films using long spin times or tert-butyl alcohol as a solvent," *PLoS One*, 2009, doi: 10.1371/journal.pone.0004572.
- [10] A. W. Martinez, S. T. Phillips, G. M. Whitesides, and E. Carrilho, "Diagnostics for the developing world: Microfluidic paper-based analytical devices," *Anal. Chem.*, 2010, doi: 10.1021/ac9013989.
- [11] A. K. Yetisen, M. S. Akram, and C. R. Lowe, "Paper-based microfluidic point-of-care diagnostic devices," *Lab on a Chip*, 2013, doi: 10.1039/c3lc50169h.
- [12] P. Hazarika, D. Chowdhury, and A. Chattopadhyay, "Fabrication of submicron scale patterned plastic thin film fluidic devices with controllable thickness," *Lab a Chip - Miniaturisation Chem. Biol.*, 2003, doi: 10.1039/b302563m.
- [13] M. Focke, D. Kosse, C. Müller, H. Reinecke, R. Zengerle, and F. Von Stetten, "Lab-on-a-Foil: Microfluidics on thin and flexible films," *Lab on a Chip*, 2010, doi: 10.1039/c001195a.
- [14] Y. Yalikul, Y. Hosokawa, T. Iino, and Y. Tanaka, "An all-glass 12 μm ultra-thin and flexible micro-fluidic chip fabricated by femtosecond laser processing," *Lab Chip*, 2016, doi: 10.1039/c6lc00132g.
- [15] Y. Hanada, K. Sugioka, I. Miyamoto, and K. Midorikawa, "Double-pulse irradiation by laser-induced plasma-assisted ablation (LIPAA) and mechanisms study," in *Applied Surface Science*, 2005, doi: 10.1016/j.apsusc.2005.03.050.
- [16] M. S. Plesset and A. Prosperetti, "Bubble Dynamics and Cavitation," *Annu. Rev. Fluid Mech.*, vol. 9, no. 1, pp. 145–185, Jan. 1977, doi: 10.1146/annurev.fl.09.010177.001045.
- [17] M. Farhat, A. Chakravarty, and J. E. Field, "Luminescence from hydrodynamic cavitation," *Proc. R. Soc. A Math. Phys. Eng. Sci.*, vol. 467, no. 2126, pp. 591–606, 2011, doi: 10.1098/rspa.2010.0134.
- [18] K. Manmi and Q. Wang, "Acoustic microbubble dynamics with viscous effects," *Ultrason. Sonochem.*, vol. 36, pp. 427–436, 2017, doi: 10.1016/j.ulsonch.2016.11.032.
- [19] Q. Wang, "Local energy of a bubble system and its loss due to acoustic radiation," *J. Fluid Mech.*, vol. 797, no. 2016, pp. 201–230, 2016, doi: 10.1017/jfm.2016.281.
- [20] J. R. Dormand and P. J. Prince, "A family of embedded Runge-Kutta formulae," *J. Comput. Appl. Math.*, 1980, doi: 10.1016/0771-050X(80)90013-3.
- [21] J. Rapet, Y. Tagawa, and C. D. Ohl, "Shear-wave generation from cavitation in soft solids," *Appl. Phys. Lett.*, vol. 114, no. 12, 2019, doi: 10.1063/1.5083141.
- [22] E. A. Brujan and A. Vogel, "Stress wave emission and cavitation bubble dynamics by nanosecond optical breakdown in a tissue phantom," *J. Fluid Mech.*, vol. 558, pp. 281–308, 2006, doi: 10.1017/S0022112006000115.
- [23] R. Timm, "Optical and acoustic investigations of the dynamics of laser-produced cavitation bubbles near a solid boundary," *J. Fluid Mech.*, 1989, doi: 10.1017/S0022112089002314.
- [24] W. Soliman, T. Nakano, N. Takada, and K. Sasaki, "Modification of Rayleigh-Plesset theory for reproducing dynamics of cavitation bubbles in liquid-phase laser ablation," *Jpn. J. Appl. Phys.*, vol. 49, no. 11, 2010, doi: 10.1143/JJAP.49.116202.
- [25] Q. Wang, "Multi-oscillations of a bubble in a compressible liquid near a rigid boundary," *J. Fluid Mech.*, vol. 745, pp. 509–536, 2014, doi: 10.1017/jfm.2014.105.
- [26] T. Iino *et al.*, "High-speed microparticle isolation unlimited by Poisson statistics," *Lab Chip*, 2019, doi: 10.1039/c9lc00324j.
- [27] Y. Hosokawa, M. Hagiya, T. Iino, Y. Murakami, and A. Ito, "Noncontact estimation of intercellular breaking force using a femtosecond laser impulse quantified by atomic force microscopy," pp. 1–6, 2010, doi: 10.1073/pnas.1006847108.
- [28] Y. Yalikul, Y. Hosokawa, T. Iino, and Y. Tanaka, "An all-glass 12 μm ultra-thin and flexible micro-fluidic chip fabricated by femtosecond laser processing," *Lab Chip*, vol. 16, no. 13, pp. 2427–2433, 2016, doi: 10.1039/c6lc00132g.
- [29] Y. Yalikul, N. Tanaka, Y. Hosokawa, T. Iino, and Y. Tanaka, "Ultrathin glass filter fabricated by femtosecond laser processing for high-throughput microparticle filtering," *Appl. Phys. Express*, vol. 9, no. 6, p. 066702, Jun. 2016, doi: 10.7567/APEX.9.066702.